PCCP

ROYAL SOCIETY OF CHEMISTRY

PAPER

View Article Online
View Journal | View Issue

Cite this: *Phys. Chem. Chem. Phys.*, 2024, **26**, 11414

Evaluating mAbs binding abilities to Omicron subvariant RBDs: implications for selecting effective mAb therapies†

Song Luo, Danyang Xiong, Bolin Tang, Bangyu Liu, Xiaoyu Zhao and Lili Duan *

The ongoing evolution of the Omicron lineage of SARS-CoV-2 has led to the emergence of subvariants that pose challenges to antibody neutralization. Understanding the binding dynamics between the receptor-binding domains (RBD) of these subvariants spike and monoclonal antibodies (mAbs) is pivotal for elucidating the mechanisms of immune escape and for advancing the development of therapeutic antibodies. This study focused on the RBD regions of Omicron subvariants BA.2, BA.5, BF.7, and XBB.1.5, employing molecular dynamics simulations to unravel their binding mechanisms with a panel of six mAbs, and subsequently analyzing the origins of immune escape from energetic and structural perspectives. Our results indicated that the antibody LY-COV1404 maintained binding affinities across all studied systems, suggesting the resilience of certain antibodies against variant-induced immune escape, as seen with the mAb 1D1-Fab. The newly identified mAb 002-S21F2 showed a similar efficacy profile to LY-COV1404, though with a slightly reduced binding to BF.7. In parallel, mAb REGN-10933 emerged as a potential therapeutic candidate against BF.7 and XBB.1.5, reflecting the importance of identifying variant-specific antibody interactions, akin to the binding optimization observed in BA.4/5 and XBB.1.5. And key residues that facilitate RBD-mAb binding were identified (T345, L441, K444, V445, and T500), alongside residues that hinder protein–protein interactions (D420, L455, K440, and S446). Particularly noteworthy was the inhibited binding of V445 and R509 with mAbs in the presence of mAb 002-S21F2, suggesting a mechanism for immune escape, especially through the reduction of V445 hydrophobicity. These findings enhance our comprehension of the binding interactions between mAbs and RBDs, contributing to the understanding of immune escape mechanisms. They also lay the groundwork for the design and optimization of antiviral drugs and have significant implications for the development of treatments against current and future coronaviruses.

Received 4th December 2023,
Accepted 21st March 2024

DOI: 10.1039/d3cp05893j

rsc.li/pccp

Introduction

Over time, SARS-CoV-2 has acquired genetic mutations, leading to several variants and subvariants that have been confirmed. Certain variants have garnered significant attention due to their rapid transmission, enhanced immune evasion, and severity of infection, and are considered to pose a public health threat. In November 2021, Botswana reported the first case of the Omicron variant (B.1.1.529), known for its enhanced immune evasion.[1–3] It quickly spread to several other countries worldwide. Subsequently, due to Omicron's replication advantages and continued lineage evolution, subvariants emerged that were not only more transmissible but also more capable of evading antibodies, gradually replacing previous dominant sublineages.[4–7]

Starting with BA.2, several subvariants appeared rapidly in succession, often several at a time.[8,9] BA.2.12.1 emerged in the United States in early February 2022 and has significantly spread, now accounting for over 55% of all new SARS-CoV-2 infections in the country. BA.4 and BA.5 appeared in South Africa in January 2022 and quickly dominated, with a total frequency exceeding 88%.[10] These include the BA.4 and BA.5 subvariants (with the same spike protein, referred to as BA.4/5), which have risen to dominance and shown further immune evasion. The SARS-CoV-2 Omicron subvariants BA.2 and BA.4/5 have significantly surged, becoming dominant in the United States and South Africa, respectively, with BA.4/5 currently being the most widespread and influential variant.[11]

School of Physics and Electronics, Shandong Normal University, Jinan, 250014, China. E-mail: duanll@sdnu.edu.cn

† Electronic supplementary information (ESI) available: The information on relative binding free energy of specific residues calculated by using ASIE methods. See DOI: https://doi.org/10.1039/d3cp05893j

The continued evolution of Omicron and the subsequent emergence of subvariants, which are not only more transmissible but also more adept at antibody evasion, have raised concerns. These subvariants, carrying additional mutations in the spike protein, may further evade neutralizing antibodies, potentially undermining the efficacy of COVID-19 vaccines and therapeutic monoclonal antibodies. Many subvariants have emerged, evading vaccine and infection-induced immunity, showing strong immune evasion in humans. Notably, the BA.4/5 and BA.2.75 subvariants have driven the further diversified spread of SARS-CoV-2, leading to several additional subvariants, including BA.4.6, BF.7 (BA.5.2.17), BQ.1, and BQ.1.1 (derived from BA.4/5), as well as BA.2.75.2 (derived from BA.2.75). Moreover, the frequencies of these new subvariants are currently increasing and may become the next major dominant Omicron sublineages.

In October 2022, the Omicron subvariant BF.7 became the most infectious strain within the Omicron family in China, distinct from other subvariants.[12–14] BF.7 exhibited stronger immune evasion, a shorter incubation period, and a faster transmission rate. The surge in COVID-19 cases associated with BF.7 in China and other countries has triggered a global alert. Molecular modeling studies have revealed potential mechanisms for antibody immune evasion mediated by mutations K444T, F486S, and D1199N on the receptor-binding domain (RBD).[15] However, studies indicate that the Omicron subvariant BF.7 carries additional specific mutations, namely R346T in the SARS-CoV-2 RBD spike protein, originating from the BA.4/5 subvariants. Consequently, the BF.7 variant exhibits a 4.4-fold higher resistance to neutralization compared to the original D614G variant.[15] The Arg346 mutation R346T in the BF.7 variant spike, particularly in the RBD, is associated with increased immune evasion capabilities, neutralizing antibodies produced by vaccines or previous infections. This variant shows significant resistance to most currently available monoclonal antibodies and polyclonal plasma from individuals vaccinated and recently recovered from Omicron COVID-19 infections (VaxCCP).[15,16]

Recently, the XBB subvariant has acquired two additional mutations in the spike protein, including G252V (XBB.1) and G252V + S486P (XBB.1.5).[17,18] The impact of these mutations on XBB.1.5 is not yet fully understood. Given the rapid increase in the circulation of XBB.1.5 and XBB.1.16 in the United States and other parts of the world, understanding their impact on current public health measures is crucial.

New variants of the virus continue to pose a significant concern, and it was crucial to conduct research on the implications of new mutations for effective treatment.[19,20] Wang *et al.* found that antibody bebtelovimab (LY-COV1404, a fully human immunoglobulin G1 (IgG1) monoclonal SARS-CoV-2 antibody targeting the RBD with authorization for clinical treatment) showed good efficacy against the BA.2.12.1 and BA.4/5 subvariants *in vitro*.[21] REGN-10987 (imdevimab) and REGN-10933 (casirivimab) as combined antibodies showed limited efficacy against BA.2.12.1 and BA.4/5. Kumar *et al.* identified an RBD-specific mAb 002-S21F2 with rare gene usage,[22,23] which efficiently neutralized live virus isolates of SARS-CoV-2 variants. Nikhil Maroli and colleagues examined the binding of RBDs of the SARS-CoV-2, categorized as single (N501Y), double (E484Q and L452R), and triple mutations (N501Y, E484Q, and L452R), with ACE2. They found that double and triple mutations exhibited stronger binding, potentially contributing to higher transmissibility of the new variants. Additionally, their investigation into the binding of the B38 monoclonal antibody revealed limited conformational changes in the RBD and the ACE2 receptor, attributable to their effective binding interactions.[24,25] Despite our understanding of the binding capabilities of several mAbs, little is known about their efficacy against variants such as BF.7 and XBB.1.5. To gain a deeper understanding of the capabilities and limitations of these mAbs, it is critical to explore their properties. This knowledge would facilitate the development of more effective treatments for diseases.

Boonkrai *et al.* have successfully generated human monoclonal antibodies using hybridoma technology. The antibodies 1D1 and 3D2, intended for use in cocktail therapies, have been found to target non-competitive epitopes on the RBD, demonstrating neutralizing activity against the wild-type Alpha, Beta, Gamma, Delta variants.[26] Current studies indicate that the asparagine residue (N) 32 of the 1D1 Fab forms a hydrogen bond with A475 of the SARS-CoV-2 RBD.[27] Therefore, substituting alanine with valine at this position could disrupt the interaction and reduce the binding of mAb 1D1 to the BA.5 spike. It was also discovered that despite the disruption of the hydrogen bond between A475 and N32 by the A475V mutation, 1D1 retains its neutralizing ability against the BA.2 spike. This particular mechanism has greatly piqued our research interest.

In addition, ABBV-47D11 is a full-length human immunoglobulin G1 (IgG1) monoclonal antibody with an unmodified Fc region, targeting a conserved epitope within the SARS-CoV-2 S1B domain, which is distal to the ACE2 binding site on the surface spike protein of SARS-CoV-2. The S protein of SARS-CoV-2 consists of two main structural domains: S1, which includes the N-terminal domain and the receptor-binding domain S1B.[28] ABBV-47D11 targets a conserved epitope in the SARS-CoV-2 S1B domain, leading to the neutralization of SARS-CoV-2 *in vitro* and *in vivo*. ABBV-47D11 has been shown to effectively inhibit SARS-CoV-2 infection in VeroE6 cells with a 50% inhibitory concentration (IC50) of 0.57 $\mu g\ ml^{-1}$.[28–30] Whether ABBV-47D11 can neutralize Omicron subvariants remains to be demonstrated through extensive research.

In this study, the binding affinity of the six aforementioned monoclonal antibodies to Omicron subvariants BA.2, BA.4/5, BF.7, and XBB.1.5 was predicted. Molecular dynamics simulations were employed to discern whether mutations contribute to immune escape and to explore the potential mechanisms involved.

Methods

(1) Molecular dynamics simulations

The structures of the complexes used in this work to predict and analyze the specificity of the RBDs of spike proteins and six

mAbs, and the WT structures were obtained from the protein data bank (PDB) database, with PBD coding for 8D8Q, 8D8R, 6XDG, 7UPL, 8BSE, and 7AKD, respectively. The focus of our study is on predicting the binding affinity of six mAbs to SARS-CoV-2 Omicron subvariants BA.2, BA.4/5, BF.7, and XBB.1.5 through molecular dynamics simulations. By predicting the binding free energy, we aim to assess the strength of the interaction and thereby evaluate the potential for immune escape due to mutations in the RBD of spike. Therefore, preprocessing of the system, including making initial PDB file adjustments to retain only the RBD region and the antibody structures (RBD residues range from 334–527), is required before performing the dynamics simulations. The LEaP module of AMBER18[31] software was used to construct residue libraries and force field parameters. All the standard residues were mutated using the LEaP module of AMBER18 to obtain their initial structures for dynamics simulation according to the mutation information of Table 1.

Before carrying out the dynamics simulations, the parameters of the protein and mAbs were prepared using the AMBER18 protein ff14SB force field. The missing hydrogen atoms in the initial structure were added through the LEaP module in the AMBER 18 package. A truncated octahedron periodic water box of TIP3P water was added to create a solvent environment, and a reasonable buffer distance of 10 Å was set. Additionally, counter ions were added to make the whole system appear electrically neutral. Subsequently, the steepest descent method was used to minimize the energy of the entire system followed by the conjugate gradient minimization to make the system reach convergence. Then, each system was heated from 0 to 300 K for 1 ns with a weak restraint of (10 kcal mol^{-1} $Å^{-2}$) and the bonds involving hydrogen atoms were constrained by the SHAKE algorithm,[32] and the Langevin dynamics[33] with a collision frequency of 1 ps^{-1} used to maintain the temperature.

In this study, we opted for a 10 × 100 ns simulation strategy in the *NPT* ensemble. The initial conformation for each simulation was taken from the last frame of the previous simulation, with random velocities reassigned. This approach allowed us to monitor for any significant conformational changes within the system at any given time. The total simulation time amounted to 1 μs. As observed in the last two simulations, the system's root mean square deviation (RMSD) had stabilized, leading to the use of the final 200 ns of trajectory for energy and conformational analysis. Trajectories were recorded every 10 ps, resulting in a total of 20 000 frames.

(2) MM/GBSA method

In this work, the MM/GBSA method was employed to calculate the binding free energy of the systems. During the calculation, the binding free energy was divided into two parts, enthalpy change (ΔH) and entropic contribution ($-T\Delta S$), and thereby the following equation was obtained:

$$\Delta G = \Delta H - T\Delta S \quad (1)$$

Enthalpy change included two parts, the solvation free energy (ΔG_{sol}) and the ensemble-average protein–ligand interaction energy ($\langle E_{pl}^{int} \rangle$). At the same time, $\langle E_{pl}^{int} \rangle$ could also be divided into two parts, electrostatic interaction (ΔE_{ele}) and vdW interaction (ΔE_{vdw}).

Besides, the solvation free energy (ΔG_{sol}) can be separated into the polar solvation free energy (ΔG_{gb}) and the non-polar solvation free energy (ΔG_{np}). Therefore, eqn (1) can finally be described using the following formula:

$$\Delta G_{bind} = \Delta E_{ele} + \Delta E_{vdw} + \Delta G_{pb/gb} + \Delta E_{np} - T\Delta S \quad (2)$$

ΔG_{gb} is calculated using the Generalized Born (GB) equation and the ΔG_{np} is calculated using the empirical formula,

$$\Delta G_{np} = \gamma \cdot \mathrm{SASA} + \beta \quad (3)$$

where SASA is the solvent-accessible surface area, which is obtained using the MSMS program.

(3) Interaction entropy (IE) method

The entropy change is calculated using the IE method in this work. In this method, the entropy change is defined by the following equation:

$$-T\Delta S = KT \ln \left\langle e^{\beta \Delta E_{pl}^{int}} \right\rangle \quad (4)$$

where β is equal to $\frac{1}{KT}$ and ΔE_{pl}^{int} is the fluctuation of the protein–ligand interaction energy relative to the average interaction energy ($\langle E_{pl}^{int} \rangle$) so that the following equation is obtained.

$$\Delta E_{pl}^{int} = E_{pl}^{int} - \langle E_{pl}^{int} \rangle \quad (5)$$

Table 1 Detailed mutation information of the RBD region of spike protein of Omicron variants. (From: https://covid19dashboard.regeneron.com/content/1/?tab=Lineage_Details)

Lineage	WHO label	First seen	Location first seen	Mutations
BA.2	Omicron	2020/3/28	France	G339D, S371F, S373P, S375F, T376A, D405N, R408S, K417N, N440K, S477N, T478K, E484A, Q493R, Q498R, N501Y, Y505H
BA.4/BA.5	Omicron	2020/6/30	Mauritius	G339D, S371F, S373P, S375F, T376A, D405N, R408S, K417N, N440K, L452R, S477N, T478K, E484A, F486V, Q498R, N501Y, Y505H
BF.7	Omicron	2022/1/2	France	G339D, R346T, S371F, S373P, S375F, T376A, D405N, R408S, K417N, N440K, L452R, S477N, T478K, E484A, F486V, Q498R, N501Y, Y505H
XBB.1.5	Omicron	2020/4/4	United States (North Carolina)	G339H, R346T, L368I, S371F, S373P, S375F, T376A, D405N, R408S, K417N, N440K, V445P, G446S, N460K, S477N, T478K, E484A, F486P, F490S, Q498R, N501Y, Y505H

$\langle E_{pl}^{int} \rangle$ and $\left\langle e^{\beta \Delta E_{pl}^{int}} \right\rangle$ can be calculated using the formulas:

$$\left\langle E_{pl}^{int} \right\rangle = \frac{1}{T}\int_0^T E_{pl}^{int}(t)dt = \frac{1}{N}\sum_{i=1}^{N} E_{pl}^{int}(t_i) \quad (6)$$

and

$$\left\langle e^{\beta \Delta E_{pl}^{int}} \right\rangle = \frac{1}{N}\sum_{i=1}^{N} e^{\beta \Delta E_{pl}^{int}(t_i)} \quad (7)$$

(4) ASGB combined with the interaction entropy method[34] (ASIE)

Alanine scanning is used to evaluate the contribution of individual residues to binding. Amino acids within 10 Å of the binding interface are mutated separately to structurally simple alanine, and the difference in the energy of the system before and after the mutation is considered as the energy contribution of specific residues. It calculates the difference in binding free energy of the system before and after mutation by mutating a specific residue (x) to alanine (a) one by one:

$$\Delta\Delta G_{bind}^{x \to a} = \Delta G_{bind}^{x} - \Delta G_{bind}^{a} \quad (8)$$

According to eqn (1), the binding free energy is divided into an enthalpy term (ΔH) and an entropy term ($-T\Delta S$), so eqn (8) can be further expressed as

$$\begin{aligned}\Delta\Delta G_{bind}^{x \to a} &= (\Delta H^{x} - T\Delta S^{x}) - (\Delta H^{a} - T\Delta S^{a}) \\ &= \Delta\Delta H^{x \to a} - T\Delta\Delta S^{x \to a}\end{aligned} \quad (9)$$

For the ASIE method, the enthalpy part is calculated using MM/GBSA and the entropy contribution is calculated using the IE method, respectively.

Results and discussion

In this study, we investigated the binding effects of these six mAbs aforementioned mAbs on Omicron subvariants, including wild type (WT), BA.2, BA.4/5, BF.7, and XBB.1.5, and assessed whether these mAbs showed any signs of immune escape, and the structures of SARS-CoV-2 and the spike protein are shown in Fig. 1A. Table 1 shows the detailed information of the RBD's mutation sites of the above mutants. And Fig. 2 shows the binding conformations of six antibodies and mutants, with the mutation sites highlighted in orange. Based on the initial conformation observations, it is noted that both 10 933 and 10 987 exhibit limited contact with the RBD. mAb 47D11 has a smaller number of residues, totaling only 226 residues across two chains. This is significantly few compared to the residue counts of five other mAbs, which range from 429 to 439. This will also be a factor that affects the binding energy of 47D11 to RBD.

Energy calculations of antibody systems

LY-COV1404. Table 2 presents the detailed binding free energy values along with the enthalpic contribution calculated using molecular mechanics/Generalized Born surface area (MM/GBSA)[35–40] and the entropic contribution obtained through the interaction entropy (IE) method.[41–43] These values were predicted during the final 200 ns of a 1 μs molecular dynamics[44,45] simulation scale. From Table 2, LY-COV1404 maintained a strong binding ability to several Omicron variants, albeit with a slight decrease in the binding free energy compared to the WT. Notably, the binding ability between LY-COV1404 and BF.7/XBB.1.5 was significantly weakened, with binding energies of only −7.11 and −6.46 kcal mol^{-1}, respectively. However, no immune escape phenomenon was observed, indicating that LY-COV1404 could be used for the treatment of

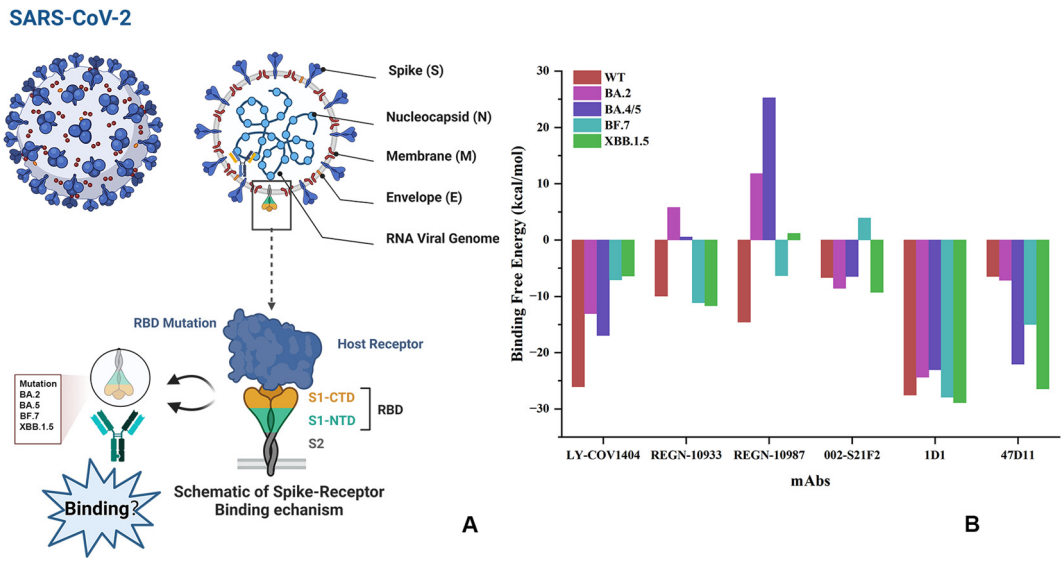

Fig. 1 (A) Structural depiction of SARS-CoV-2 and the interaction between the receptor-binding domain (RBD) and an antibody, created with BioRender.com. (B) Binding free energies of mAbs with the RBD from various Omicron subvariants including WT, BA.2, BA.4/5, BF.7 and XBB.1.5. All values are in kcal mol^{-1}.

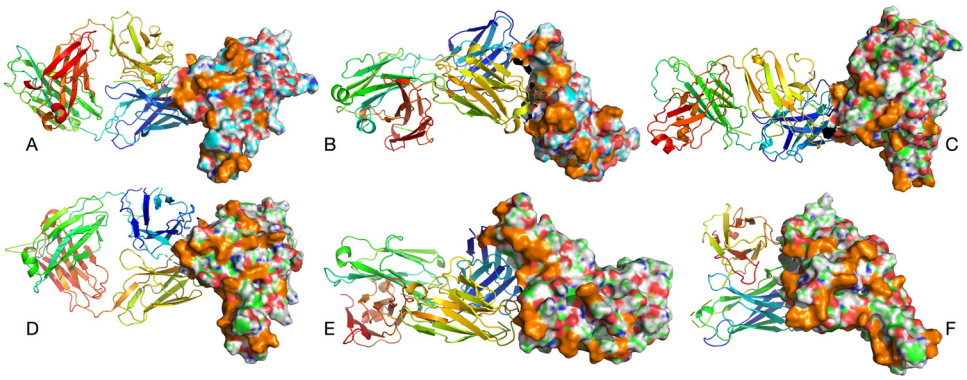

Fig. 2 The structural conformation of each mAbs and RBD. (A) LY-COV1404, (B) REGN-10933, (C) REGN-10987, (D) 002-S21F2, (E) 1D1, (F) 47D11, the antibody is displayed in a new cartoon style, and the RBD is displayed in a surface. The mutation site studied in this work in the RBD region is displayed in orange.

Table 2 Binding free energy components of mAbs against Omicron, enthalpic contribution obtained by MM/GBSA and entropic contribution calculated through interaction entropy method, all values are in kcal mol^{-1}

mAbs	Omicron	ΔE_{ele}	ΔE_{vdW}	$\Delta G_{solv,pol}$	$\Delta G_{solv,np}$	ΔH	$-T\Delta S$	ΔG_{bind}
LY-COV1404	WT	−191.68 ± 6.27	−83.32 ± 0.62	199.45 ± 4.42	−12.37 ± 0.04	−87.92 ± 0.66	61.85	−26.07 ± 0.66
	BA.2	−256.78 ± 14.49	−84.53 ± 1.34	253.09 ± 15.01	−13.17 ± 0.21	−101.39 ± 1.62	88.31	−13.08 ± 1.62
	BA.4/5	−263.55 ± 21.18	−89.53 ± 2.4	271.63 ± 18.56	−13.10 ± 0.32	−94.54 ± 2.79	77.56	−16.98 ± 2.79
	BF.7	−255.61 ± 0.93	−78.95 ± 0.50	258.00 ± 1.95	−12.04 ± 0.11	−88.61 ± 2.17	81.50	−7.11 ± 2.17
	XBB.1.5	−208.28 ± 2.03	−79.43 ± 2.04	219.02 ± 3.24	−12.20 ± ±0.14	−80.89 ± 2.34	74.43	−6.46 ± 2.34
REGN-10933	WT	−111.33 ± 0.71	−63.03 ± 0.91	135.86 ± 0.42	−11.08 ± 0.18	−49.57 ± 2.26	39.59	−9.98 ± 2.26
	BA.2	−176.51 ± 13.47	−80.74 ± 0.65	196.61 ± 12.32	−13.03 ± 0.27	−73.66 ± 2.07	79.42	5.76 ± 2.07
	BA.4/5	−222.12 ± 1.63	−78.01 ± 0.06	239.35 ± 0.76	−12.91 ± 0.28	−73.68 ± 0.75	74.21	0.51 ± 0.75
	BF.7	−227.86 ± 1.63	−85.50 ± 0.95	249.55 ± 1.31	−13.59 ± 0.12	−77.39 ± 2.82	66.26	−11.13 ± 2.82
	XBB.1.5	−158.59 ± 7.79	−87.95 ± 4.85	177.89 ± 7.53	−13.86 ± 0.50	−82.45 ± 4.48	70.80	−11.65 ± 4.48
REGN-10987	WT	−82.53 ± 8.65	−94.14 ± 0.92	122.87 ± 8.11	−14.12 ± 0.03	−67.90 ± 0.54	53.34	−14.56 ± 0.54
	BA.2	−11.96 ± 5.54	−78.74 ± 0.29	35.43 ± 2.27	−13.08 ± 1.01	−68.20 ± 1.94	79.98	11.78 ± 1.94
	BA.4/5	98.19 ± 7.18	−65.03 ± 6.15	−65.72 ± 2.72	−10.27 ± 1.01	−42.84 ± 0.45	68.06	25.22 ± 0.45
	BF.7	137.46 ± 7.23	−86.56 ± 0.44	−110.06 ± 5.10	−13.38 ± 0.01	−72.54 ± 0.75	66.19	−6.35 ± 0.75
	XBB.1.5	171.53 ± 6.79	−88.95 ± 1.84	−129.26 ± 6.70	−12.19 ± 0.37	−58.87 ± 1.19	60.02	1.16 ± 1.19
002−S21F2	WT	−258.24 ± 14.11	−80.84 ± 2.36	279.46 ± 13.44	−12.69 ± 0.29	−72.30 ± 5.97	65.59	−6.72 ± 5.97
	BA.2	−359.74 ± 4.53	−77.08 ± 0.71	375.35 ± 3.04	−12.30 ± 0.03	−73.76 ± 1.50	65.22	−8.55 ± 1.50
	BA.4/5	−310.83 ± 5.76	−79.90 ± 0.19	336.81 ± 5.80	−13.05 ± 0.01	−66.97 ± 1.28	60.45	−6.52 ± 1.28
	BF.7	−276.81 ± 1.08	−66.77 ± 1.35	295.81 ± 0.21	−11.10 ± 0.19	−59.36 ± 3.24	63.25	3.89 ± 3.24
	XBB.1.5	−232.43 ± 6.16	−70.12 ± 0.89	247.91 ± 4.21	−10.99 ± 0.12	−65.59 ± 2.99	56.33	−9.27 ± 2.99
1D1	WT	−214.34 ± 0.92	−86.55 ± 0.88	228.70 ± 2.76	−14.49 ± 0.01	−86.68 ± 0.94	59.13	−27.55 ± 4.04
	BA.2	−212.77 ± 14.07	−88.79 ± 0.01	223.49 ± 13.66	−14.65 ± 0.22	−92.71 ± 0.63	68.32	−24.39 ± 2.44
	BA.4/5	−185.59 ± 0.69	−83.75 ± 0.01	197.34 ± 1.23	−13.58 ± 0.05	−85.57 ± 0.59	62.50	−23.07 ± 1.41
	BF.7	−198.53 ± 10.05	−84.22 ± 0.47	210.43 ± 11.07	−13.74 ± 0.19	−86.06 ± 0.35	58.12	−27.94 ± 1.34
	XBB.1.5	−149.69 ± 7.35	−85.18 ± 0.11	159.65 ± 7.16	−13.65 ± 0.08	−88.87 ± 0.01	59.96	−28.91 ± 1.02
47D11	WT	−72.04 ± 3.31	−85.17 ± 0.73	110.39 ± 6.55	−12.81 ± 0.09	−57.62 ± 0.40	51.09	−6.52 ± 3.95
	BA.2	−89.39 ± 18.12	−85.36 ± 0.03	123.83 ± 11.62	−13.64 ± 0.54	−64.57 ± 5.92	57.37	−7.19 ± 3.98
	BA.4/5	−94.82 ± 2.26	−95.59 ± 1.29	125.93 ± 1.48	−13.91 ± 0.04	−78.40 ± 2.03	56.32	−22.08 ± 6.63
	BF.7	−84.02 ± 19.12	−84.86 ± 7.88	112.99 ± 11.77	−12.75 ± 1.01	−68.64 ± 1.53	53.64	−15.00 ± 2.96
	XBB.1.5	−39.83 ± 0.09	−104.95 ± 1.50	85.62 ± 0.05	−15.44 ± 0.13	−74.59 ± 1.77	48.13	−26.46 ± 1.84

BF.7 and XBB.1.5, albeit with a potentially reduced therapeutic effect compared to its use against BA.2 and BA.4/5.

REGN-10933 and REGN-10987. The predicted results for REGN-10933 and REGN-10987 were consistent with the work of Wang *et al.*[21] Both antibodies failed to maintain a strong binding ability to BA.2 and BA.4/5, particularly the REGN-10933-BA.2 (REGN-10933-BA.4/5) system, as shown in Fig. 1B, which presents a histogram of the binding free energies for various systems, primarily to compare the predicted binding energies across these systems. The specific values of the binding energies are provided in Table 2. In addition, molecular dynamics (MD) simulations revealed a significant change in the electrostatic energy compared to WT, from −111.33 to −176.51 and −222.12 kcal mol^{-1}, for REGN-10933-BA.2 and REGN-

10933-BA.4/5 system, respectively, with a large fluctuation in the interaction energy. The result of binding free energy suggested that there may be a lack of intrinsic driving force for the two mAbs binding to BA.2/BA.4/5. Moreover, dynamic sampling statistics on the angle between RBD, heavy chain and light chain ($\angle\alpha$) indicated significant deviation of the RBD from the binding interface, with the angle changing from 37.24° to 118.22° (79.30°) compared to the WT. This angle reflects the degree of deviation in various mutant antibodies. By analyzing the offset distance, we can infer the binding trend of the antibody with the RBD caused by mutations, thereby determining whether the binding conformation is tighter or looser, which helps to assess whether the antibody has a tendency for immune escape (Fig. 3).

Based on the results of binding free energy calculations, it appears that both REGN-10933 and BF.7/XBB.1.5, with an

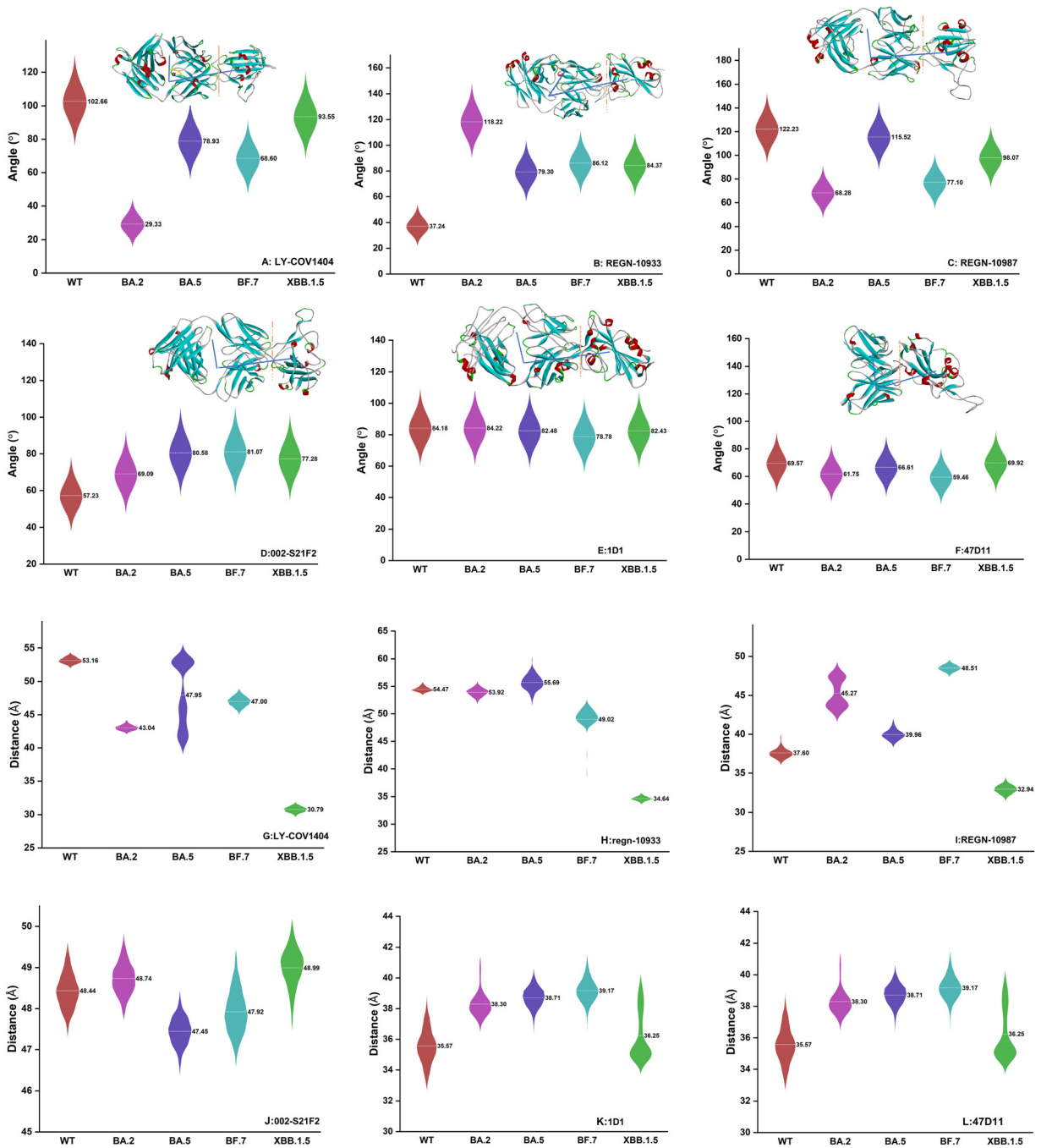

Fig. 3 Angle between RBD, heavy, and light chains of mAbs (A) LY-COV1404, (B) REGN-10933, (C) REGN-10987, (D) 002-S21F2, (E) 1D1, (F) 47D11, with colors of numbers indicating different Omicron subvariants. And mass distance between RBD and heavy chains is shown for (G) LY-COV1404, (H) REGN-10933, (I) REGN-10987, (J) 002-S21F2, (K) 1D1, (L) 47D11.

energy of −11.13 and −11.65 kcal mol^{-1}, respectively, have a stronger enthalpy contribution and smaller entropy loss when compared to BA.2 and BA.4/5. This indicates that REGN-10 933 may be a potential treatment option for BF.7/XBB.1.5. The stronger binding affinity of REGN-10933 and BF.7/XBB.1.5 can be attributed to the shorter mass distance between the RBD and the heavy chain, which is significantly lower than that of BA.2 and BA.4/5. (Fig. 3H) The greater binding affinity observed with REGN-10933 and BF.7/XBB.1.5 is likely due to the closer proximity between the RBD and the heavy chain. This allows for more frequent interactions and thus, a more stable binding.

REGN-10987 did not exhibit immune escape to BF.7, but the predicted binding free energy suggests that it may not be suitable for treating XBB.1.5. Compared to REGN-10933, it had weaker binding ability to BF.7 (−6.35 *vs.* −11.13 kcal mol^{-1}). A newly discovered mAb, 002-S21F2, targets RBD and effectively inhibits BA.2 and BA.4/5, similar to LY-COV1404. In all 002-S21F2-RBD systems analyzed, the mass distances between heavy chain and RBD exhibit minimal variation (Fig. 3J), indicating the stability of the 002-S21F2-Omicron system combination. Additionally, this result suggests that differences between the systems have little effect on this stability. Few mAbs can target multiple Omicron subvariants due to the immune escape phenomenon, but 002-S21F2 and LY-COV1404 has potential and requires further clinical trials.

002-S21F2. Moreover, 002-S21F2 exhibits strong binding affinity to the RBD of XBB.1.5, second only to REGN-10933 among the four studied mAbs systems. Extended MD simulations revealed that the average angle between RBD, heavy, and light chains of mAbs, (Fig. 3D) which was found to be 81.07° for 002-S21F2 and BF.7, indicates that this antibody faces challenges in maintaining a stable binding conformation. This instability ultimately leads to deflection and compromises its ability to effectively bind to the targets.

1D1-Fab. In the present study, 1D1-Fab emerged as a unique antibody among the six analyzed for its consistent binding free energy across four SARS-CoV-2 variants and the WT, without demonstrating immune escape in the context of the Omicron variant. The calculated binding free energies, while numerically distinct across the variants, showed relatively small disparities, as exemplified by the comparison of the WT with a binding free energy of −27.55 kcal mol^{-1} to XBB.1.5, which displayed the minimal observed difference at −28.91 kcal mol^{-1}. It was notable that the XBB.1.5 variant, while displaying the most stable binding free energy with the antibody, differs from WT by a mere 1.36 kcal mol^{-1}. Additionally, the binding free energies of the BA.2 and BA.4/5 variants, at −24.39 kcal mol^{-1} and −23.07 kcal mol^{-1} respectively, while elevated compared to WT, remain within a similar magnitude. These data suggested that despite surface characteristic alterations due to mutation, antibody recognition and binding to these variants remain highly effective, implying a lack of significant immune escape between 1D1-Fab and the variants. Data indicate that the WT exhibits the most negative electrostatic interactions (−214.34 kcal mol^{-1}), indicative of strong Coulombic interactions, with its vdW interactions (−86.545 kcal mol^{-1}) also demonstrating strong non-covalent interactions. Nevertheless, the total binding free energy for WT (−27.55 kcal mol^{-1}) is not the most negative, possibly reflecting the influence of other complex interactions beyond electrostatic and vdW forces on the system's stability. Compared to other variants, XBB.1.5 shows the lowest binding free energy (−28.91 kcal mol^{-1}), suggesting that thermodynamically it may form the most stable antibody–variant complex. This finding does not correlate exactly with its electrostatic interaction value (−149.69 kcal mol^{-1}), which is not the most negative among all variants. This result implies that the binding free energy is not solely determined by electrostatic and vdW contributions but is the result of a composite of forces. Other variants, such as BA.2 and BA.4/5, with binding free energies of −24.39 kcal mol^{-1} and −23.07 kcal mol^{-1}, respectively, are higher than WT and XBB.1.5, indicating a lower binding affinity with the antibody. BA.4/5, in particular, with the highest binding free energy, exhibits the weakest binding affinity, potentially linked to its less favorable electrostatic interactions (−185.59 kcal mol^{-1}) and vdW forces (−83.75 kcal mol^{-1}).

The subtle differences in binding free energies may reflect minor changes in the microenvironment of the binding site of the variants, including rearrangements of amino acid side chains, fine-tuning of polar and non-polar areas, and possible reorganization of hydrogen-bond networks. However, these changes have not resulted in a significant thermodynamic disadvantage in binding to the antibody. Therefore, despite changes in the molecular details of interaction, the antibody has maintained a sufficient level of resilience in its overall binding capability to these variants.

From the perspective of binding free energies, there appears to be no significant immune escape of the variants with 1D1-Fab. However, a comprehensive assessment of the antibody's neutralizing ability against the mutated proteins and the binding mechanism requires an integrated consideration of multiple analytical approaches.

47D11. Our detailed binding free energy analysis across various SARS-CoV-2 variants with 47D11 has revealed distinct interaction profiles. The WT exhibits moderate electrostatic interactions (−72.04 kcal mol^{-1}) and vdW forces (−85.165 kcal mol^{-1}), culminating in a relatively higher overall binding free energy (−6.525 kcal mol^{-1}). This indicates that the mutations alter the charge distribution around the binding site, enhancing the electrostatic interactions between 47D11 and the BA.2, BA.4/5, BF.7 variants, thereby facilitating its binding with the mutants.

For the BA.2 variant, an enhancement in electrostatic interactions (−89.39 kcal mol^{-1}) over the WT is observed, yet this change does not significantly lower the binding free energy (−7.20 kcal mol^{-1}), indicating that the increase in electrostatic attraction is not sufficient to notably improve antibody binding affinity.

Remarkably, the BA.4/5 variant displays the strongest electrostatic (−94.82 kcal mol^{-1}) and vdW (−95.59 kcal mol^{-1}) interactions, with a substantially reduced binding free energy (−22.08 kcal mol^{-1}). This means that the mutations not only significantly enhance the electrostatic attraction at the binding

site but also lead to a more compact spatial configuration. Such a tighter binding between the antibody and the RBD demonstrates increased binding affinity and stability, fully illustrating the positive impact of the mutations on the binding efficacy. In contrast, the BF.7 variant, with its binding free energy (-15.00 kcal mol^{-1}), shows moderate antibody binding affinity, implying that this variant may have undergone adjustments in the charge distribution and hydrophobic contact points to maintain sufficient antibody interaction. The entropy change analysis suggests that binding processes involve differences in dynamics. The higher entropy change in BA.2 indicates a possibility of increased conformational freedom during binding, or a greater number of water molecules being displaced from the binding interface.

The data on XBB.1.5 are particularly enlightening. Despite its electrostatic interactions (-39.83 kcal mol^{-1}) being considerably weaker than other variants, a significantly negative vdW interaction (-104.95 kcal mol^{-1}) leads to a low binding free energy of -26.46 kcal mol^{-1}. This exceptional value suggests that for XBB.1.5, vdW forces play a decisive role in antibody binding, possibly due to unique hydrophobic regions or tight molecular contacts.

Through evaluated the binding abilities of the six mAbs to various Omicron subvariant RBDs (BA.2, BA.4/5, BF.7, XBB.1.5), it's observed that LY-COV1404 displayed a significant degree of binding affinity to all subvariants, while REGN-10933 had the potential to treat BF.7 and XBB.1.5, and REGN-10987 showed weakened binding ability to BF.7. Among the mAbs, 002-S21F2 showed similar performance to LY-COV1404, but stronger binding ability to BF.7 was not observed. The 1D1-Fab antibody demonstrates a remarkable consistency in binding affinity across a range of SARS-CoV-2 variants, indicating no significant immune escape and suggesting a robust neutralizing potential against these variants. And in-depth analysis reveals that while the WT variant shows moderate interaction strength, variants such as BA.4/5 and XBB.1.5 exhibit optimized binding site environments leading to significantly stronger antibody interactions, with vdW forces playing a crucial role for XBB.1.5. More detailed interaction details and factors that induce immune escape should be further discussed.

Overall, these findings provide a nuanced view of the thermodynamic parameters governing the interactions between the variants and the antibody, offering valuable insights into predicting antibody neutralization potential and understanding potential immune escape mechanisms of the variants. However, calculations of binding free energy alone are insufficient to fully evaluate these interactions; combining structural analysis with dynamic simulations will provide a more comprehensive and accurate understanding.

Residue decomposition analysis: dissecting the systems

Some of the spike proteins of coronaviruses exhibit homology, such as MERS-CoV, SARS-CoV, and SARS-CoV-2. The RBDs of these three viruses share similarities in structure and sequence, particularly SARS-CoV and SARS-CoV-2, which have a higher degree of similarity. Identifying the key residues involved in the binding of spike protein/mAbs and analyzing the amino acids that exhibit significant changes in binding affinity upon spike protein mutation are crucial for understanding the binding mechanisms between mAbs and Omicron subvariants. In this work, alanine scanning combined with the interaction entropy method (ASIE)[34,46,47] can be employed to determine the energetic contributions of specific residues within a protein. This approach effectively mitigates potential systematic errors stemming from trajectory mutations, thereby offering an advantage in evaluating the relative contributions of binding free energy among residues. As we all known, Omicron variants has similar RBD structures and only few residues was different, thus the role of the residues can be investigated using the ASIE approach. Therefore, in this study, the binding free energies of residues were evaluated (Fig. 4 and Tables S1–S6, ESI†), within a 10 Å range from binding interface. For the values calculating through ASIE, positive values indicate a favorable contribution towards antibody–protein binding, while negative values suggest a detrimental effect.

Although the sequence of Omicron variants is similar, the residues scanned by ASIE include the specific mutant sites. So, for the sake of simplicity, the sequences in Fig. 4 are based on the wild-type (WT), and the mutant residues are explained in the legend.

For LY-COV1404, residues 444, 445, and 500 of RBDs exhibited stronger energy contributions when interacting with WT, BA.2, BA.4/5, BF.7, and XBB.1.5. Except for K444, which had a binding free energy contribution of 1.20 kcal mol^{-1} in the XBB.1.5/LY-COV1404 interaction, the other two residues had binding energy contributions greater than 2 kcal mol^{-1} in any of the systems (K444/V445 in WT, BA.2, and BA.4/5, P445 in XBB.1.5, T500 in all RBDs). As the positively charged residue, K444 exhibited significant electrostatic interactions in all systems (7.53 to 10.18 kcal mol^{-1}). Additionally, the hydrophobicity of V445 ensured stable binding between RBDs and LY-COV1404, accompanied by pronounced binding free energy contributions (3.50 to 4.42 kcal mol^{-1}). As a neutral amino acid, the van der Waals (vdW) interactions of T500 with LY-COV1404 were the primary energy contribution, surpassing the contribution from electrostatic interactions. For example, in the BA.2 system, the vdW energy contributed from T500 was stronger than the electrostatic energy by 3.08 kcal mol^{-1} (3.39 *vs.* 0.31 kcal mol^{-1}). Furthermore, when binding to LY-COV1404, T500 showed minimal entropy changes in all Omicron variants investigated in this study, suggesting that significant conformational changes were unlikely to occur. In addition to the notable contributions of residues 444, 445, and 500 to the binding of LY-COV1404, energy analysis of the residues revealed that K440 had almost no energy contribution in the BA.4/5 system but exhibited strong hindrance to binding in other systems. From an energy and conformational perspective, it can be inferred that K440 deviated from the binding pocket structure in BA.4/5, leading to a decrease in all energy terms. And similar deviation was observed for R498 in BF.7, which was also the important residue should be focus on.

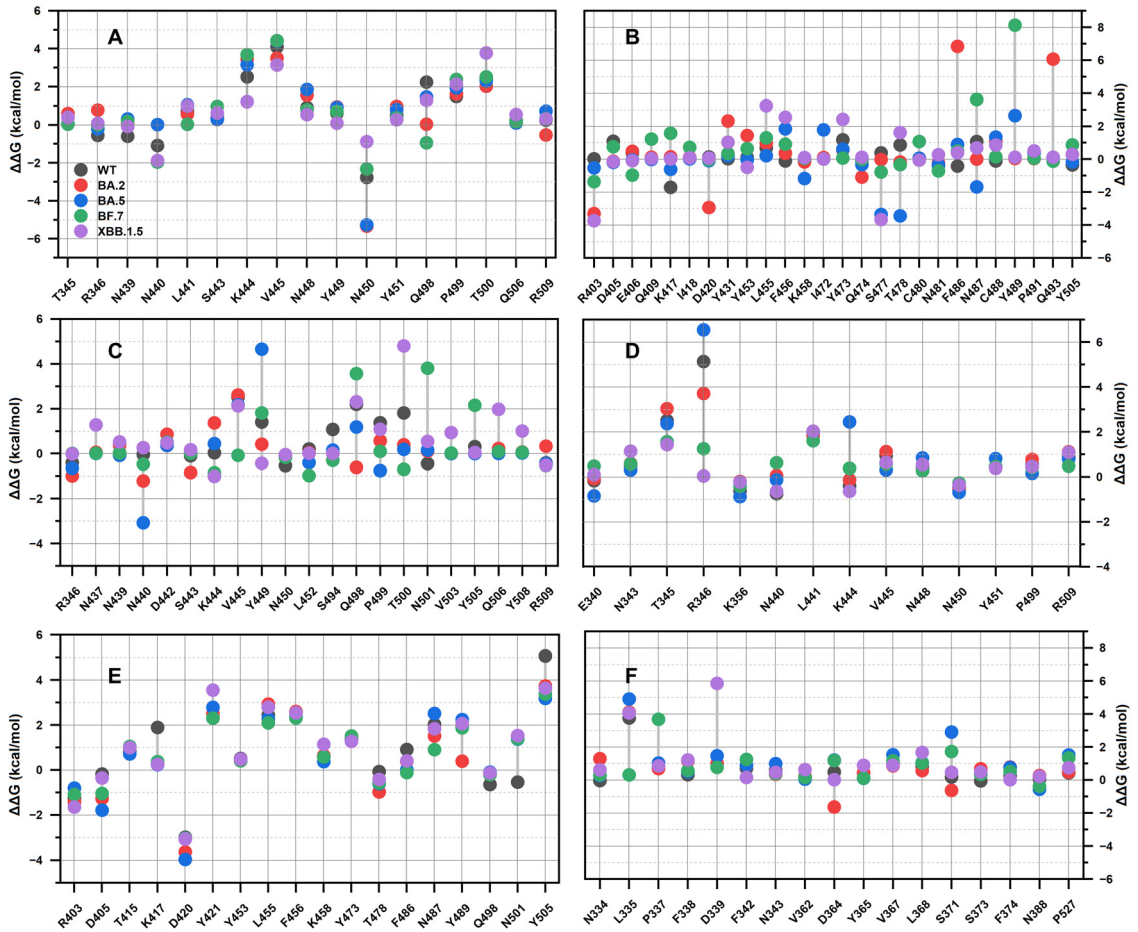

Fig. 4 Contribution of residues to binding free energy calculated through the ASIE method, (A) LY-COV1404, (B) REGN-10933, (C) REGN-10987, (D) 002-S21F2, (E) 1D1, (F) 47D11. Residue names are referenced to the WT, where the residues are mutated: N405, N417, K440, N477, K478, R498, Y501, H505 in BA.2, BA.5, BF.7, and XBB.1.5, T346 in XBB.1.5 and BF.7, P445 in XBB.1.5, R494 in BA.2, V486 in BA.5 and BF.7, P486 in XBB.1.5, R452 in BA.5 and BF.7.

For REGN-10933, no residues were found with an energy contribution greater than 2 kcal mol^{-1} in any system, and the reduced energy contribution of multiple residues contributed to the immune escape observed in BA.2 and BA.4/5. Consequently, it was challenging to identify hotspot residues (binding free energy contribution >2 kcal mol^{-1}) that consistently contribute to binding across all systems. By examining the energy changes of residues, some insights can be gained into the reasons underlying the immune escape phenomenon. D420 in BA.2, exhibited a pronounced hindering effect on RBD and antibody binding, with a binding free energy contribution of -2.95 kcal mol^{-1}, and this negative effect was not observed in other systems. Analysis of the energy components of D420 revealed a significant entropic contribution (-3.35 kcal mol^{-1}) upon alanine mutation, indicating that the unstable conformation of this residue during binding to REGN-10933 may lead to immune escape. Similarly, L455 in BF.7/XBB.1.5 showed strong binding free energy contributions, with values of 1.29 kcal mol^{-1} and 3.23 kcal mol^{-1}, respectively, while exhibiting weaker energy contributions in BA.2 and BA.4/5 (0.96 and 0.20 kcal mol^{-1}, respectively). This disparity contributes to the immune escape phenomenon observed in BA.2 and BA.4/5. Another residue with the similar role is Q474, which hindered RBDs and REGN-10933 binding in BA.2 and BA.4/5 (-1.10 and -0.35 kcal mol^{-1}, respectively).

Meanwhile, no hotspot residues were found during the binding of REGN-10987/RBDs in each system. And immune escape was also observed with REGN-10987, as its binding free energies were consistently weak in BA.2, BA.4/5, and XBB.1.5, which was explained in the energy analysis (binding affinity predicted through MM/GBSA). While analyzing the residues involved in binding with REGN-10987, S446, a unique residue, was exclusively identified in the REGN-10987/XBB.1.5 system through ASIE. When using the ASIE method, residues unscanned were considered no contribution to the binding of the RBD to the mAbs. When scanning the RBDs binding to REGN-10987, S446 was not detected in WT, BA.2, BA.5, or BF.7, but residues S443 and K444 (near the S446) were observed. This suggested that the center of mass of S446 was beyond the scanning range, and its side chain should undergo deviation to be recognized, contributing significantly to the binding with XBB.1.5 (2.14 kcal mol^{-1}). In future studies on the antibody-XBB.1.5 binding characteristics,

particular attention may be given to this residue. Furthermore, K440 was found to exhibit a stronger inhibitory effect in BA.2 and BA.4/5, with energies contributions of -1.22 kcal mol^{-1} and -3.08 kcal mol^{-1}, respectively. Additionally, the hydrophobic effect of V445 was suppressed in BF.7, causing the significant decrease in binding free energy compared to the WT with REGN-10987. Results also revealed that the weakened vdW interactions made R498 an inhibitory residue.

During the scanning of RBDs with 002-S21F2, the fewest number of residues was found among all mAbs-RBD complexes. Immune escape was only observed in the BF.7 system, which can be attributed to the overall weaker energy contributions of the residues in this system and the minimal number of "warm spot" residues ($1 < \Delta\Delta G < 2$ kcal mol^{-1}). Residues T345 and L441 were identified as stable residues promoted mAbs-RBDs binding in all systems, with fluctuating binding free energy contributions ranging from 1.43 to 3.03 kcal mol^{-1} and 1.60 to 2.03 kcal mol^{-1}, respectively. When designing novel mAbs, it is crucial to ensure the energy contribution of these residues to the binding. Additionally, residue 346, originally an arginine (R346, in WT, BA.2, and BA.4/5), exhibited stronger binding free energy contributions in all systems (3.71 to 6.54 kcal mol^{-1}). However, after mutating to threonine (T346, in BF.7, and XBB.1.5), a significant decrease of that was observed, with values of 1.24 kcal mol^{-1} and 0.04 kcal mol^{-1} in BF.7 and XBB.1.5, respectively. When dealing with RBDs from similar coronaviruses in the future, the contributions of R346 can be considered for selecting suitable mAbs. In the 002-S21F2/BF.7 system, where immune escape occurred, it was found that the hydrophobic effect of residue V445 at the binding interface was suppressed, and the relatively weak of contribution of R509 to binding free energy induced the immune escape.

In our investigation of 1D1-Fab's interaction with various Omicron subvariants, free energy analysis has led to the conclusion that there is no significant enhancement in the antibody's ability to escape immune detection across these variants. A detailed decomposition of the energetic contributions of individual residues to protein binding offers insights into this observation. Despite differences in mutation sites, most key residues contribute similarly across variants, with only a few displaying variations. For instance, residues R403 and D420 inhibit binding in all variants with an energy contribution of approximately -1 kcal mol^{-1}. Conversely, residues Y421, L455, F456, and Y473 facilitate binding, each contributing over 1 kcal mol^{-1}, a consistency that suggests these differences are unlikely to cause substantial changes in the binding affinity.

However, some residues do exhibit variant-specific energy contributions. Notably, Y489 has a lower contribution in the BA.2 complex at just 0.39 kcal mol^{-1}, compared to a minimum of 1.87 kcal mol^{-1} in other variants, primarily due to a significant increase in entropy loss, indicating greater instability of this residue in the 1D1-BA.2 complex. Additionally, the D405N mutation exhibits a more pronounced inhibitory effect on binding, where despite favorable changes in electrostatic energy, there is an accompanying increase in the entropy loss. The mutation T478K significantly reduces electrostatic energy, thereby mainly contributing to the inhibition of protein–antibody binding.

These findings imply that while there are differences in the energetic contributions of certain residues among the Omicron subvariants, they do not fundamentally affect the binding energy of 1D1-Fab. The action of residues that positively contribute to binding energy may counterbalance those with significant variations. Such detailed residue-level analysis enhances our understanding of the complexities of protein–antibody interactions.

In previous studies, the 47D11 antibody demonstrated weaker binding affinity with the WT and BA.2 variants, while binding most strongly to the XBB.1.5 variant with an energy of -26.46 kcal mol^{-1}. This compels a more in-depth analysis from the perspective of residue decomposition to ascertain the causes of binding energy variations among systems. Scanning residues within a 10 Å radius of the antibody-spike binding interface revealed that while residue 339 is absent in the WT, it contributes positively to binding in other variants, with the smallest contribution in BA.2 at 0.99 kcal mol^{-1}, and the largest in XBB.1.5 at 5.85 kcal mol^{-1}, directly affecting its binding affinity. Additionally, residue L335 consistently acts as a hotspot in binding across systems, with its lowest energy contribution in the BF.7 system at 3.67 kcal mol^{-1}, mainly attributed to vdW forces, indicating more atomic contacts and interactions with the antibody. Another factor leading to weaker binding energies in WT and BA.2 is the lower energy contributions of residues S371 and D364, constrained by lower electrostatic energies and greater entropy losses. Targeted antibody optimization on these residues may yield monoclonal antibodies with enhanced inhibitory effects.

In summary, analysis of residue contributions to binding free energy during the interaction between mAbs and RBDs, showed that several key residues played a critical role in binding enhancement (*e.g.*, K444, V445, and T500 in RBD binding with LY-COV1404; T345 and L441 in RBD binding with 002-S21F2) and some residues inducing immune escape (*e.g.*, D420 and L455 in RBDs/REGN-10933; K440 and S446 in RBDs/REGN-10987; V445 and R509 in RBDs/002-S21F2) had been identified. These findings would contribute to the understanding of the binding mechanisms between the six mAbs and the Omicron variants and provide insights into the factors that induce immune escape phenomena caused by specific residues.

Cluster analysis: categorizing residues in each system

For the convenience of comparing and describing the relationships between different residues of systems, hierarchical clustering analysis was performed based on the ASIE results in this work (Fig. 5). In different systems, residues that exhibit similar energy contributions can be classified into a single category to investigate the shared characteristics and differences in the roles these residues play across various mutants. This approach allows for a systematic comparison of how specific amino acid

residues influence the binding affinity and overall stability of the protein complex in different mutational contexts. Based on the comparison of binding free energies for the same residues, the LY-COV1404/RBDs system can be categorized into two groups. The first group consists of WT, BA.2, and BA.5, while the second group includes BF.7 and XBB.1.5. The grouping results were consistent with those of REGN-10987/RBDs and 002-S21F2/RBDs, indicating that although different mAbs were used to inhibit the Omicron variant, the relative energy distribution of residues in RBDs was similar. The clustering of residues based on their energy levels is presented on the left side of each subplot in Fig. 5. Residues within groups a1, b1, c4, and d1 predominantly exhibited inhibitory effects on binding, while residues in groups a3, b2, b3, c1, c2, d2, and d3 contributed favorably to binding. The clustering results clearly differentiated the roles played by residues in different systems. Notably, for the mAbs/XBB.1.5 systems, residues N450, T500, and Q506 exhibited favorable contributions to binding when interacting with LY-COV1404, while they acted as inhibitory residues in other RBDs. Similar cases can be observed in groups b1, c4, and d1. Residues K444, V445, N448, Y449, and Y451 showed unfavorable contributions in LY-COV1404/XBB.1.5 but acted as favorable residues in other RBDs. Through hierarchical clustering analysis, it provides a more intuitive perspective for a comprehensive understanding of the performance of amino acid. These residues that played opposite roles in different systems affect the neutralization of antibodies and should be paid more attention. From Fig. 5(E) and (F), we can clearly discern the significant differences in residue contributions among different systems, as previously analyzed. When employing the ASGB method for residue analysis, it was observed that for the 1D1, most residues contribute similarly to the RBDs, resulting in minimal energy differences between the variants. (e1) However, in the case of 47D11 binding to BA.2, there were fewer residues making favorable contributions, and these contributions were relatively weak. This phenomenon was likely the primary reason for the notable differences in binding energies between 47D11 and BF.7, and XBB.1.5.

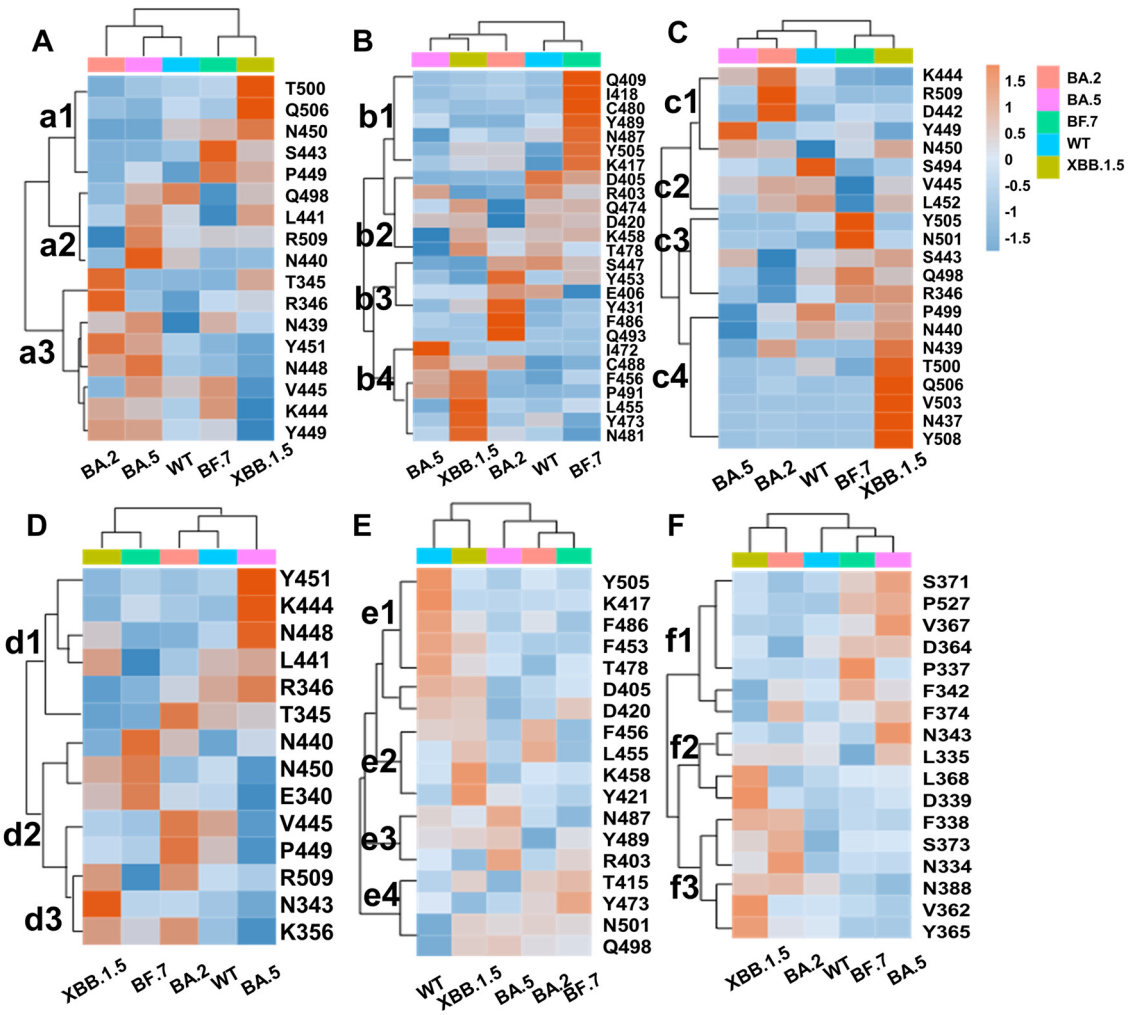

Fig. 5 Hierarchical cluster analysis for residues, which binding free energy calculated through ASIE method, (A) LY-COV1404, (B) REGN-10933, (C) REGN-10987, (D) 002-S21F2, (E) 1FD1, (F) 47D11. Residue names are referenced to the WT, where the residues are mutated as mentioned in Fig. 3. And this figure was plotted by **https://www.bioinformatics.com.cn**, an online platform for data analysis and visualization.

Hydrogen bond network analysis

As a protein–antibody system, the binding interface exhibits more residue contacts and atomic interactions compared to the protein–ligand system. Proteins and antibodies were more likely to form an extensive hydrogen bond network. Investigating the changes in the hydrogen bond network caused by mutations could provide insights into the potential variations in complex stability. Through analyzing the formation and disruption of hydrogen bonds and the number of stable hydrogen bonds, the binding affinity between proteins and antibodies can be assessed. Therefore, in the subsequent work, the hydrogen bond networks in various systems were analyzed. (Fig. 6)

Firstly, the number of hydrogen bonds with an occupancy percentage above 60% during the dynamic process was calculated. For the LY-COV1404/RBDs system, most hydrogen bonds were observed in the BA.2 complex, with an increase of 5 hydrogen bonds compared to the WT. This increase was reflected in the electrostatic interaction energy, which was stronger by 65.10 kcal mol^{-1}, changing from −191.68 to −256.78 kcal mol^{-1}. The stable hydrogen bond numbers in other systems were similar, ranging from 5 to 7 bonds. And the results shows that the hydrogen bond T53@O···V445@H-V445@N and G447@O···R59@H-R59@N were broken in XBB.1.5 and BA.5, respectively, while showed high occupancy percentage in other systems (Fig. 6B). The REGN-10933/BF.7 complex exhibited the highest number of hydrogen bonds among all systems, showing the strongest electrostatic energy (−227.86 kcal mol^{-1}) when interacting with REGN-10933. Additionally, the presence of a larger number of stable hydrogen bonds, which could promote the binding conformational stabilization, was one of the reasons why REGN-10933 did not show immune escape in the BF.7 complex. Additionally, the REGN-10933/BA.2 complex had 12 stable hydrogen bonds, implying a relatively stable binding as well. However, energy calculations over time revealed a fluctuation in the electrostatic energy, primarily due to the presence of five hydrogen bonds with lower occupancy percentages (60% to 70%), leading to a larger entropic contribution and a weaker binding affinity.

Among the REGN-10987/RBDs systems, the REGN-10987/BA.5 complex showed the lowest number of hydrogen bonds, followed by REGN-10987/BA.2, and then REGN-10987/XBB.1.5, indicating a stronger correlation with the immune escape observed in these three systems. For the 002-S21F2/RBDs system, WT, BA.2, BA.5, and BF.7 had a similar number of hydrogen bonds (7 to 9). Only 002-S21F2/XBB.1.5 exhibited a lower number of hydrogen bonds (5), but three of them with occupancy percentages exceeding 90%, shorter bond distances (2.79 to 3.10 Å), and larger bond angles (160.47 to 164.38°), contributed to the stability and higher energy of these hydrogen bonds. Moreover, these factors facilitated the formation of a stable complex between the 002-S21F2 and XBB.1.5, ensuring a reduced likelihood of dissociation from the pocket. As a result, it effectively mitigated the risk of immune escape, thereby enhancing the overall effectiveness of the treatment.

When compared to other antibodies, 1D1 was found to have the highest number of stable hydrogen bonds in its interaction with the spikes. Even with the BA.4/5 variant, 1D1-spike still had the most hydrogen bonds compared to other mAbs.[17] In the binding with the wild-type (WT) variant, the numbers of hydrogen bonds exceeding 60% totals 26, and those over 90% reach 13, indicating a high occupancy of hydrogen bonds. This distribution of stable hydrogen bonds suggested that these systems possess strong binding free energy and stable binding conformations. The subtle variations observed imply that the binding capacity of 1D1 across different systems may not significantly differ and suggest that the 1D1 interaction with these variants was comparatively stable and might exhibit potent neutralizing capabilities.

On the other hand, the binding affinity of antibody 47D11 with WT and BA.2 was inferred to be weaker due to fewer hydrogen bonds. Both WT and BA.2 have only one hydrogen bond when binding with this mAb, suggesting lower stability in these interactions compared to other variants. Notably, compared to BA.5 and XBB.1.5, the hydrogen bond numbers increase to 9 and 8, respectively, which may reflect a higher affinity of 47D11 towards the specific mutation sites of these variants. The enhancement in affinity could be attributed

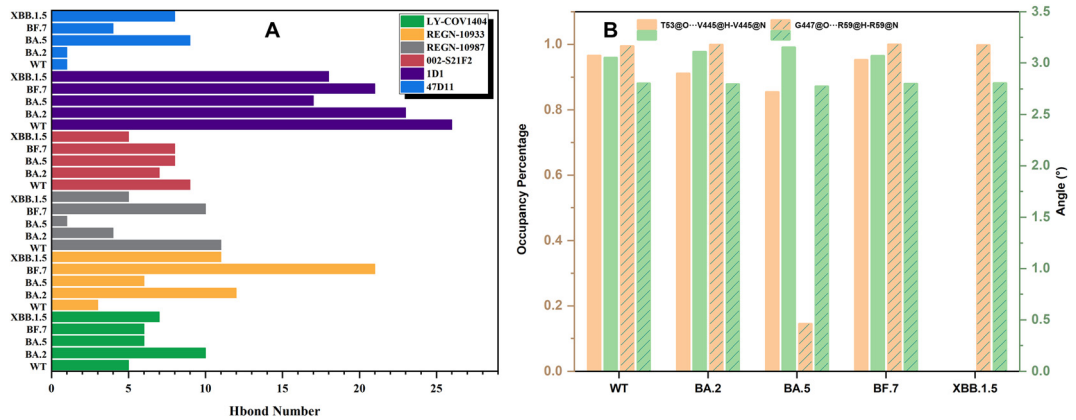

Fig. 6 (A) Number of hydrogen bonds for mAbs/RBDs systems, (B) The occupancy percentages (origin) and bond angles (green) of hydrogen bonds (T53@O···V445@H-V445@N, and G447@O···R59@H-R59@N) in LY-COV1404/RBDs.

to changes in specific residues critical to hydrogen bond formation.

It is crucial to recognize that the number of hydrogen bonds does not necessarily correlate directly with the strength of binding affinity, as other non-covalent interactions, such as hydrophobic effects, ionic bonds, and vdW forces, also play roles in the stability of the complex. Nonetheless, the quantity of hydrogen bonds serves as a useful indicator for guiding subsequent experimental designs and theoretical simulations. In summary, the data suggested that antibody 1D1 may possess broader neutralizing activity, whereas antibody 47D11 may be more effective against specific variants, such as BA.5 and XBB.1.5.

The insights gained by analyzing hydrogen bonds were essential for understanding how mutations affect antibody recognition and were practical for designing therapeutic strategies that can combat emerging variants with broad-spectrum or highly specific antibodies.

Conclusions

Since the evolution of the SARS-CoV-2 Omicron variant has led to the emergence of subvariants that can evade antibody recognition, this study focused on investigating the binding mechanisms between six mAbs and the Omicron subvariants of SARS-CoV-2, aiming to predict the potential for immune escape and explore the reasons behind it using reliable dynamic approaches and accurate binding free energy predicted methods, from an energetic and structural perspective.

The results showed that LY-COV1404 could bind to the RBDs of all Omicron subvariants studied in this work, and the newly discovered mAb 002-S21F2 exhibited similar binding characteristics to LY-COV1404 but with weaker binding to BF.7. Additionally, the REGN-10933 also showed potential for treating BF.7 and XBB.1.5. By analyzing the energy contributions of RBD residues, several amino acids that play a crucial role in promoting binding, such as T345, L441, K444, V445, and T500, were identified. Residues with inhibitory effects on binding, such as D420, L455, K440, and S446, were also determined.

Furthermore, immune escape was observed in the 002-S21F2/BF.7 system, in which V445 and R509 exhibiting inhibited binding to the antibody compared to other 002-S21F2-RBDs systems, particularly because the hydrophobicity of V445 was inhibited at the binding interface. This study provides important insights into the binding modes between antibodies and RBDs and the factors contributing to immune escape.

From the perspective of binding free energy analysis, 1D1-Fab demonstrates consistent immunological responses across multiple variants, with no significant evidence of immune escape. In all variants examined, residues R403 and D420 uniformly exhibited an inhibitory effect on antibody binding, each contributing approximately -1 kcal mol^{-1} to the energy profile. Conversely, residues Y421, L455, F456, and Y473 universally enhanced binding across all variants, with contributions exceeding 1 kcal mol^{-1} each, indicating that their role is unlikely to induce substantial variations in binding energy. However, the neutralization efficacy of 47D11 may not be optimal against the BA.2 variant. Notably, in the XBB.1.5 variant, residue H339 makes a significant energy contribution of 5.85 kcal mol^{-1}, making it a primary factor in the robust binding energy of this system, while residue L335 consistently acts as a critical hotspot residue across all systems, underscoring its pivotal role in protein–antibody interactions.

Based on these findings, the design and optimization of antiviral drugs can be pursued to counteract immune escape of the novel coronavirus. Moreover, the study of the binding mechanisms between the RBDs of the spike protein and antibodies serves as a valuable inspiration for the future development of treatments for coronaviruses, offering guidance and strategies for the development of vaccines and antiviral drugs targeting different variants.

Conflicts of interest

The authors declare no competing interests.

Acknowledgements

This work was supported by the National Natural Science Foundation of China (grant no. 11774207).

References

1 M. Andre, L.-S. Lau, M. D. Pokharel, J. Ramelow, F. Owens, J. Souchak, J. Akkaoui, E. Ales, H. Brown, R. Shil, V. Nazaire, M. Manevski, N. P. Paul, M. Esteban-Lopez, Y. Ceyhan and N. El-Hage, *Biology*, 2023, **12**, 1267.
2 Y. Fan, X. Li, L. Zhang, S. Wan, L. Zhang and F. Zhou, *Signal Transduction Targeted Ther.*, 2022, **7**, 141.
3 R. Gili and R. Burioni, *J. Transl. Med.*, 2023, **21**, 251.
4 M. McCallum, N. Czudnochowski, L. E. Rosen, S. K. Zepeda, J. E. Bowen, A. C. Walls, K. Hauser, A. Joshi, C. Stewart, J. R. Dillen, A. E. Powell, T. I. Croll, J. Nix, H. W. Virgin, D. Corti, G. Snell and D. Veesler, *Science*, 2022, **375**, 864–868.
5 L. B. Shrestha, C. Foster, W. Rawlinson, N. Tedla and R. A. Bull, *Rev. Med. Virol.*, 2022, **32**, e2381.
6 J. Chen, R. Wang, N. B. Gilby and G.-W. Wei, *J. Chem. Inf. Model.*, 2022, **62**, 412–422.
7 D. Ao, T. Lan, X. He, J. Liu, L. Chen, D. T. Baptista-Hon, K. Zhang and X. Wei, *MedComm*, 2022, **3**, e126.
8 P. Arora, L. Zhang, C. Rocha, A. Sidarovich, A. Kempf, S. Schulz, A. Cossmann, B. Manger, E. Baier, B. Tampe, O. Moerer, S. Dickel, A. Dopfer-Jablonka, H.-M. Jäck, G. M. N. Behrens, M. S. Winkler, S. Pöhlmann and M. Hoffmann, *Lancet Infect. Dis.*, 2022, **22**, 766–767.
9 A. Rössler, A. Netzl, L. Knabl, H. Schäfer, S. H. Wilks, D. Bante, B. Falkensammer, W. Borena, D. von Laer, D. J. Smith and J. Kimpel, *Nat. Commun.*, 2022, **13**, 7701.
10 Z. Zhang, J. Mateus, C. H. Coelho, J. M. Dan, C. R. Moderbacher, R. I. Gálvez, F. H. Cortes, A. Grifoni,

A. Tarke, J. Chang, E. A. Escarrega, C. Kim, B. Goodwin, N. I. Bloom, A. Frazier, D. Weiskopf, A. Sette and S. Crotty, *Cell*, 2022, **185**, 2434–2451.e2417.

11 H. Tegally, M. Moir, J. Everatt, M. Giovanetti, C. Scheepers, E. Wilkinson, K. Subramoney, Z. Makatini, S. Moyo, D. G. Amoako, C. Baxter, C. L. Althaus, U. J. Anyaneji, D. Kekana, R. Viana, J. Giandhari, R. J. Lessells, T. Maponga, D. Maruapula, W. Choga, M. Matshaba, M. B. Mbulawa, N. Msomi, A. P. Bester, M. Claassen, D. Doolabh, I. Mudau, N. Mbhele, S. Engelbrecht, D. Goedhals, D. Hardie, N.-Y. Hsiao, A. Iranzadeh, A. Ismail, R. Joseph, A. Maharaj, B. Mahlangu, K. Mahlakwane, A. Davis, G. Marais, K. Mlisana, A. Mnguni, T. Mohale, G. Motsatsi, P. Mwangi, N. Ntuli, M. Nyaga, L. Olubayo, B. Radibe, Y. Ramphal, U. Ramphal, W. Strasheim, N. Tebeila, S. van Wyk, S. Wilson, A. G. Lucaci, S. Weaver, A. Maharaj, Y. Pillay, M. Davids, A. Mendes, S. Mayaphi, Y. Naidoo, S. Pillay, T. J. Sanko, J. E. San, L. Scott, L. Singh, N. A. Magini, P. Smith-Lawrence, W. Stevens, G. Dor, D. Tshiabuila, N. Wolter, W. Preiser, F. K. Treurnicht, M. Venter, G. Chiloane, C. McIntyre, A. O'Toole, C. Ruis, T. P. Peacock, C. Roemer, S. L. Kosakovsky Pond, C. Williamson, O. G. Pybus, J. N. Bhiman, A. Glass, D. P. Martin, B. Jackson, A. Rambaut, O. Laguda-Akingba, S. Gaseitsiwe, A. von Gottberg, T. de Oliveira and N.-S. Consortium, *Nat. Med.*, 2022, **28**, 1785–1790.

12 J. K. Singh, S. Anand and S. K. Srivastava, *Int. J. Biol. Macromol.*, 2023, **238**, 124154.

13 S. Chenchula, K. C. Amerneni, M. K. Ghanta, R. Padmavathi, M. B. Chandra, M. B. Adusumilli, M. Chavan, S. Mudda, R. Gupta and B. Lakhawat, *Virology*, 2023, **584**, 38–43.

14 F. Jian, Y. Yu, W. Song, A. Yisimayi, L. Yu, Y. Gao, N. Zhang, Y. Wang, F. Shao, X. Hao, Y. Xu, R. Jin, Y. Wang, X. S. Xie and Y. Cao, *Lancet Infect. Dis.*, 2022, **22**, 1535–1537.

15 P. Qu, J. P. Evans, J. N. Faraone, Y.-M. Zheng, C. Carlin, M. Anghelina, P. Stevens, S. Fernandez, D. Jones, G. Lozanski, A. Panchal, L. J. Saif, E. M. Oltz, K. Xu, R. J. Gumina and S.-L. Liu, *Cell Host Microbe*, 2023, **31**, 9–17.e13.

16 Q. Wang, Z. Li, J. Ho, Y. Guo, A. Y. Yeh, H. Mohri, M. Liu, M. Wang, J. Yu, J. G. Shah, J. Y. Chang, F. Herbas, M. T. Yin, M. E. Sobieszczyk, Z. Sheng, L. Liu and D. D. Ho, *Lancet Infect. Dis.*, 2022, **22**, 1666–1668.

17 D. Ao, X. He, W. Hong and X. Wei, *MedComm*, 2023, **4**, e239.

18 M. T. Kelleni, *J. Infect.*, 2023, **86**, 405.

19 E. C. Wall, M. Wu, R. Harvey, G. Kelly, S. Warchal, C. Sawyer, R. Daniels, P. Hobson, E. Hatipoglu, Y. Ngai, S. Hussain, J. Nicod, R. Goldstone, K. Ambrose, S. Hindmarsh, R. Beale, A. Riddell, S. Gamblin, M. Howell, G. Kassiotis, V. Libri, B. Williams, C. Swanton, S. Gandhi and D. L. V. Bauer, *The Lancet*, 2021, **397**, 2331–2333.

20 F. Yan and F. Gao, *J. Infect.*, 2022, **84**, 579–613.

21 H. Zhao, J. Yu, G. Q. Weng, J. H. Yu, E. C. Wang, J. B. Gao, H. X. Liu, T. J. Hou, Z. Wang and Y. Kang, *Phys. Chem. Chem. Phys.*, 2022, **25**, 15791–15801.

22 S. Kumar, A. Patel, L. Lai, C. Chakravarthy, R. Valanparambil, E. S. Reddy, K. Gottimukkala, M. E. Davis-Gardner, V. V. Edara, S. Linderman, K. Nayak, K. Dixit, P. Sharma, P. Bajpai, V. Singh, F. Frank, N. Cheedarla, H. P. Verkerke, A. S. Neish, J. D. Roback, G. Mantus, P. K. Goel, M. Rahi, C. W. Davis, J. Wrammert, S. Godbole, A. R. Henry, D. C. Douek, M. S. Suthar, R. Ahmed, E. Ortlund, A. Sharma, K. Murali-Krishna and A. Chandele, *Sci. Adv.*, 2022, **8**, eadd2032.

23 H. Ishimaru, M. Nishimura, L. H. Tjan, S. Sutandhio, M. I. Marini, G. B. Effendi, H. Shigematsu, K. Kato, N. Hasegawa, K. Aoki, Y. Kurahashi, K. Furukawa, M. Shinohara, T. Nakamura, J. Arii, T. Nagano, S. Nakamura, S. Sano, S. Iwata, S. Okamura and Y. Mori, *J. Virol.*, 2023, e00286-00223.

24 A. Aggarwal, S. Naskar, N. Maroli, B. Gorai, N. M. Dixit and P. K. Maiti, *Phys. Chem. Chem. Phys.*, 2021, **23**, 26451–26458.

25 N. Maroli, *J. Phys. Chem. B*, 2023, **127**, 8525–8536.

26 C. Boonkrai, T. S. Cotrone, W. Chaisuriyong, T. Tantawichien, U. Thisyakorn, S. Fernandez, T. Hunsawong, M. Reed, T. Wongtangprasert, T. Audomsun, T. Phakham, C. Attakitbancha, P. Saelao, D. Focht, R. Kimbung, M. Welin, A. A. Malik, T. Pisitkun and N. Srisawat, *PLoS One*, 2023, **18**, e0284173.

27 R. Viriyakitkosol, A. Wanitchang, K. Srisutthisamphan, J. Saenboonreung, C. Boonkrai, T. Pisitkun and A. Jongkaewwattana, *Front. Immunol.*, 2023, **14**, 1219546.

28 B. L. Haagmans, D. Noack, N. M. A. Okba, W. Li, C. Wang, T. Bestebroer, R. de Vries, S. Herfst, D. de Meulder, E. Verveer, P. van Run, M. M. Lamers, B. Rijnders, C. Rokx, F. van Kuppeveld, F. Grosveld, D. Drabek, C. Geurts van Kessel, M. Koopmans, B. J. Bosch, T. Kuiken and B. Rockx, *J. Infect. Dis.*, 2021, **223**, 2020–2028.

29 M. Shebley, S. Wang, I. Ali, P. Krishnan, R. Tripathi, J. M. Reardon, J. Cafardi, G. Rahav, Y. Caraco, J. Slim, F. Al Akhrass, M. Yu, Y. Hu, R. D. A. Ferreira and N. N. Alami, *Pharmacol. Res. Perspect.*, 2023, **11**, e01036.

30 C. Wang, W. Li, D. Drabek, N. M. A. Okba, R. van Haperen, A. D. M. E. Osterhaus, F. J. M. van Kuppeveld, B. L. Haagmans, F. Grosveld and B.-J. Bosch, *Nat. Commun.*, 2020, **11**, 2251.

31 D. A. Case, I. Y. B. halom, S. R. Brozell, D. S. Cerutti, T. E. Cheatham, III, V. W. D. Cruzeiro, T. A. Darden, R. E. Duke, D. Ghoreishi, M. K. Gilson, H. Gohlke, A. W. Goetz, D. Greene, R. Harris, N. Homeyer, Y. Huang, S. Izadi, A. Kovalenko, T. Kurtzman, T. S. Lee, S. LeGrand, P. Li, C. Lin, J. Liu, T. Luchko, R. Luo, D. J. Mermelstein, K. M. Merz, Y. Miao, G. Monard, C. Nguyen, H. Nguyen, I. Omelyan, A. Onufriev, F. Pan, R. Qi, D. R. Roe, A. Roitberg, C. Sagui, S. Schott-Verdugo, J. Shen, C. L. Simmerling, J. Smith, R. S. Ferrer, J. Swails, R. C. Walker, J. Wang, H. Wei, R. M. Wolf, X. Wu, L. Xiao, D. M. York and P. A. Kollman, *AMBER 2018*, University of California, San Francisco, 2018.

32 J. P. Ryckaert, G. Ciccotti and H. J. C. Berendsen, *J. Comput. Phys.*, 1977, **23**, 327–341.

33 R. W. Pastor, B. R. Brooks and A. Szabo, *Mol. Phys.*, 1988, **65**, 1409–1419.

34 X. Liu, L. Peng, Y. Zhou, Y. Zhang and J. Z. H. Zhang, *J. Chem. Theory Comput.*, 2018, **14**, 1772–1780.

35 S. Genheden and U. Ryde, *Expert. Opin. Drug. Discov.*, 2015, **10**, 449–461.
36 P. A. Kollman, I. Massova, C. Reyes, B. Kuhn, S. Huo, L. Chong, M. Lee, T. Lee, Y. Duan, W. Wang, O. Donini, P. Cieplak, J. Srinivasan, D. A. Case and T. E. Cheatham, 3rd, *Acc. Chem. Res.*, 2000, **33**, 889–897.
37 E. Wang, H. Sun, J. Wang, Z. Wang, H. Liu, J. Z. H. Zhang and T. Hou, *Chem. Rev.*, 2019, **119**, 9478–9508.
38 H. K. Srivastava and G. N. Sastry, *J. Chem. Inf. Model.*, 2012, **52**, 3088–3098.
39 G. Rastelli, A. D. Rio, G. Degliesposti and M. Sgobba, *J. Comput. Chem.*, 2010, **31**, 797–810.
40 H. Sun, Y. Li, S. Tian, L. Xu and T. Hou, *Phys. Chem. Chem. Phys.*, 2014, **16**, 16719–16729.
41 L. l Duan, X. Liu and J. Z. H. Zhang, *J. Am. Chem. Soc.*, 2016, **138**, 5722–5728.
42 K. Huang, S. Luo, Y. Cong, S. Zhong, J. Z. H. Zhang and L. Duan, *Nanoscale*, 2020, **12**, 10737–10750.
43 X. Liu, L. Peng and J. Z. H. Zhang, *J. Chem. Inf. Model.*, 2019, **59**, 272–281.
44 Y. Yue, Y. Ma, P. Qian and H. Guo, *J. Chem. Inf. Model.*, 2018, **58**, 422–429.
45 L. L. Duan, G. Q. Feng, X. W. Wang, L. Z. Wang and Q. G. Zhang, *Phys. Chem. Chem. Phys.*, 2017, **19**, 10140–10152.
46 Y. Yan, M. Yang, C. G. Ji and J. Z. H. Zhang, *J. Chem. Inf. Model.*, 2017, **57**, 1112–1122.
47 L. Qiu, Y. Yan, Z. Sun, J. Song and J. Z. H. Zhang, *Wiley Interdiscip. Rev.: Comput. Mol. Sci.*, 2018, **8**, e1342.

